Ultra-Thinned Metasurface-Embedded Smartphone Antenna-in-Package for Millimeter-Wave 5G/6G Coverage Enhancement

Jaebaek Jung, *Student Member, IEEE*, Woojun Lee, *Student Member, IEEE*, Gyuha Lee, *Graduate Student Member, IEEE*, Songcheol Hong, *Member, IEEE*, and Jungsuek Oh, *Senior Member, IEEE*

***Abstract*— In this study, we present a ultra-thinned metasurface-cased antenna-in-package (MCAiP) for a millimeter-wave (mm-wave) 5G smartphone that operates in the n257 and n258 bands of FR2 (26.5–29.5, 24.25–27.5 GHz). The proposed MCAiP consists of 1 × 4 array patch antennas, inductively loaded metasurface (ILM), a smartphone cover case made on Gorilla Glass 6 (a commonly used material), and four-channel beamforming IC; it has a thin profile of 1.63 mm, making it suitable for insertion into an actual smartphone. To validate the effectiveness of commercializing the proposed MCAiP, all the structures were fabricated using a 12-layer PCB stack-up process, and beam tilting measurement was performed using four-channel beamforming IC. The proposed AiP accomplishes a 10-dB return-loss bandwidth of 23.5–32.2 GHz and a maximum gain of 13.62 dBi. In addition, we combined the four-channel beamforming IC with a metasurface-cased antenna and conducted beam tilting measurements using the all-in-one device. The peak effective isotropic radiated power (EIRP) [dBm]/tilting degree [°] of the proposed MCAiP with an IC are 6.59/0, 5.87/12, and 3.37/27. Conversely, the beam tilting results of a nonmetasurface AiP with an IC are 2.01/0, 1.6/12, and −0.95/30. These results demonstrate that the metasurface enhances the beam coverage of the antenna.**

***Index Terms*— 5G, antenna-in-package (AiP), beam-forming IC, low-profile, metasurface, millimeter-wave (mm-wave) array antenna.**

I. Introduction

PACKAGING chip and antenna, managing multiplex antenna, and degradation of the antenna performance owing to other smartphone components, such as smartphone cover case, are examples of reported problems. Among them, the cover case effect, which deteriorates antenna performance, such as 3-D beam coverage, is surmountable. However, only a few 5G smartphone antennas in the literature deal with smartphone cover cases coupled almost directly with the antenna [1], [2], [3], [4], [5], [6], [7], [8]. Most of the reported 5G antennas in the literature have been designed while ignoring this, assuming that the design freedom in tuning geometrical antenna parameters is sufficiently high for cover packaging. To the best of our knowledge, design methodologies, topologies, and results of metasurface-cased antenna-in-package (MCAiP) incorporating the smartphone case effects have not been reported yet, while it is known that the smartphone cover case commonly degrades antenna radiation patterns. This study suggests that the proposed approach can significantly achieve beam coverage enhancement with beam steering over a broad bandwidth.

However, this considerably suppresses achievable antenna performance, such as beam coverage and peak gain (P.G). Therefore, we applied a commercial smartphone cover case, Gorilla Glass 6, on the 5G antennas. Similar to the proposed smartphone antenna, the antennas in [5] and [6] are cases where the cover case is covered near the antenna radiating part, and the antenna shown in [7] is the case where the patch antenna is designed with high-transparency ITO on the glass cover case. Finally, the antennas in [1], [2], [3], [4], and [8] are designed to radiate endfire when a metal cover case is applied. The proposed antennas have been designed, optimized, and fabricated using Gorilla Glass 6. In addition, a metasurface has been applied to improve the beam coverage of 5G smartphone antennas. The unit cell length of metasurface structures is smaller than half lambda of 28 GHz. Although research on metasurfaces has been actively conducted, it is insufficient to apply a metasurface on the AiP of a thin smartphone. Most metasurfaces applied to antennas operate as a lens that is distant from the antenna; thus, it is impossible to insert the metasurface in a smartphone. Moreover, when the distance between them is small, an air gap exists between the antennas and the metasurface, which significantly reduces the applicability of the metasurface as a real smartphone antenna component. Therefore, we developed an ultra-thinned metasurface and placed it directly on the antenna.

Manuscript received 26 September 2022; revised 11 June 2023; accepted 12 July 2023. Date of publication 8 August 2023; date of current version 6 October 2023. This work was supported in part by the Institute of Information and Communications Technology Planning and Evaluation (IITP) grant funded by the Korean Government (MSIT) (Millimeter-Wave Metasurface-Based Dual-Band Beamforming Antenna-on-Package Technology for 5G Smartphone) under Grant 2020-0-00858. *(Corresponding author: Jungsuek Oh.)*

Jaebaek Jung, Woojun Lee, and Jungsuek Oh are with the Institute of New Media and Communications (INMC) and the Department of Electrical and Computer Engineering, Seoul National University, Seoul 08826, South Korea (e-mail: jhu1988@snu.ac.kr; xxzwwe30@snu.ac.kr; jungsuek@snu.ac.kr).

Gyuha Lee and Songcheol Hong are with the Department of Electrical Engineering, Korea Advanced Institute of Science and Technology, Daejeon 34141, South Korea (e-mail: motor8888@kaist.ac.kr; schong1234@kaist.ac.kr).

Color versions of one or more figures in this article are available at https://doi.org/10.1109/TAP.2023.3301733.

Digital Object Identifier 10.1109/TAP.2023.3301733

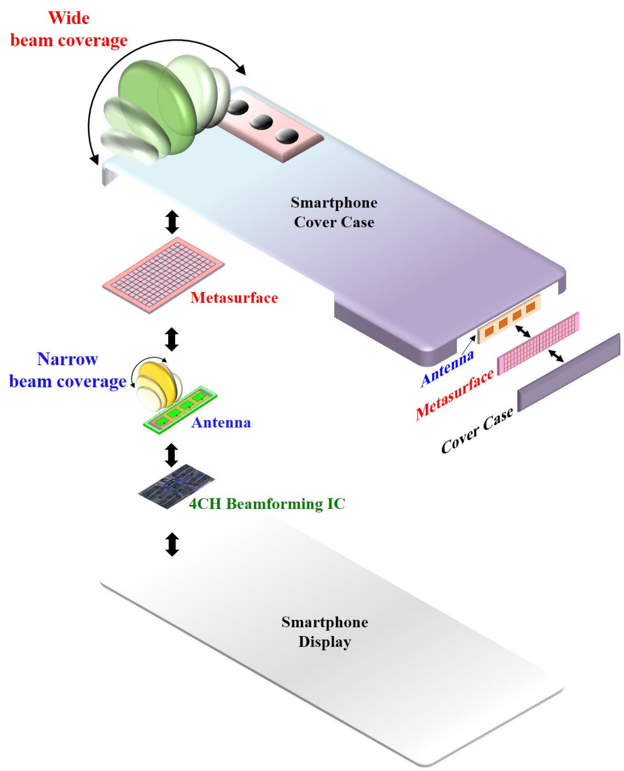

Fig. 1. Illustration of the MCAiP concept for a smartphone.

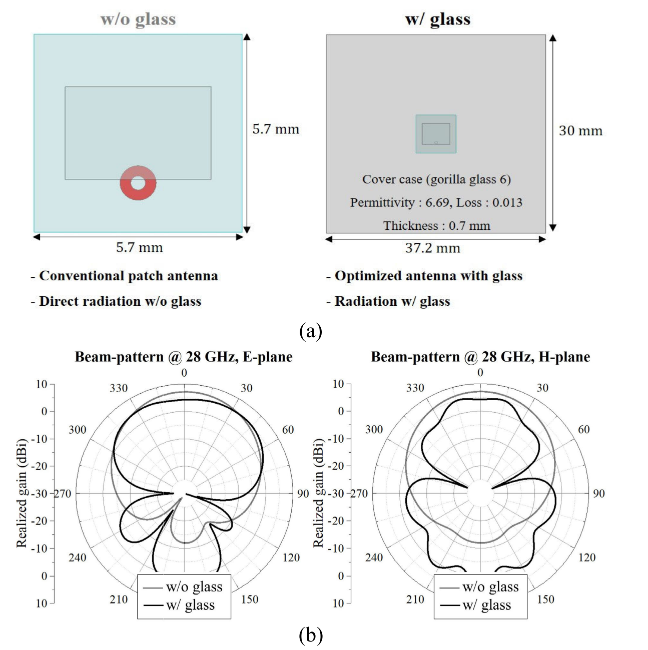

Fig. 2. Comparison of antenna performance without and with cover case (tempered glass). (a) Antenna structures. (b) Radiation patterns.

Fig. 1 shows the conceptual view of MCAiP. An IC is attached below the antenna, and the metasurface is located on the antenna; a cover case is stacked up on the metasurface. The total thickness of the combined antenna and metasurface is 1.63 mm, which fits well into an actual smartphone. As shown in Fig. 1, the ultra-thinned metasurface can be applied to either the back or side of the smartphone if the cover case covers the antenna. If the metasurface is inserted as wide as possible within the limits of the physical mounting space, the beam coverage can be maximized. The superiority of MCAiP is presented in Fig. 1. As shown in Fig. 1, the beam coverage of MCAiP is extremely wide even after being affected by the cover case. Under commercial conditions of the cover case (i.e., thickness, permittivity, and loss tangent), the metasurface and antenna are optimized to achieve the best performance of beam coverage, which is called co-design in this study. By comparing beam tilting performance or effective isotropic radiated power (EIRP) cumulative distribution function (cdf) of ultra-thinned MCAiP with those of ultra-thin dielectric spacer-cased AiP (DSCAiP), the contribution of the metasurface to beam coverage could be proved.

Based on the simulation results, Section II describes the effects of the cover case on the performance of the antenna, the modeling of a metasurface unit, and the contribution of the co-design of the cased antenna and metasurface to beam coverage. Section III shows the overall structure of a 1 × 4 array inductively loaded MCA (ILMCA) and the simulation results, which demonstrate that the beam coverage of the ILMCA is superior to that of the DSCAiP. In Section IV, the overall structure and beam tilting simulation results of a 1 × 4 array CAiP combined with a 28-GHz operating four-channel beamforming IC are introduced. Section V discusses the fabrication and measured results of CAiP. Finally, the conclusion of this study is presented in Section VI.

II. Cover Effects and Thinned Metasurface Design

In Section II-A, we analyze the effect of the cover case on the antenna coverage beam performance. Subsequently, in Section II-B, we discuss how to design a metasurface that improves THE antenna performance in combination with a cover case. The cover case applied at this time is tempered glass with a permittivity of 6.69 (Gorilla Glass 6), which is commonly used in commercial smartphones.

A. Effects of Smartphone Cover Case On Antenna

The structures of a single direct antenna without a cover case and a single antenna with a cover case are illustrated in Fig. 2(a). For simplicity, the two antennas are represented in this article as "w/o glass" and "w/ glass," respectively, and both antennas resonate at 28 GHz. Here, we focus on the effect of the cover case on the radiation pattern. The antenna's radiation pattern tends to be significantly different depending on the presence or absence of a cover case, which can be observed from the radiation pattern in Fig. 2(b) and Table I. The P.G, three-quarter gain (T.Q.G), and median gain (M.G) are the largest, three-quarters, and half values of the gain in the hemisphere in the main radiation direction of the antenna, respectively. That is, when the gain in the 3-D hemisphere is expressed as a cdf, it is a value corresponding to cdf = 1, 0.75, and 0.5. The P.G, T.Q.G, and M.G without glass are 7.1, 6.2, and 3.7 dBi, respectively, whereas those with the glass are 5.3, 4.1, and 1.8 dBi, respectively. This

TABLE I
GAINS OF THE ANTENNAS SHOWN IN FIG. 2(A) AT 28 GHz

Types of antennas	Peak gain [P.G] (dBi)	Three quarters gain [T.Q.G] (dBi)	Median gain [M.G] (dBi)	Total Eff.
w/o glass	7.1	6.2	3.7	0.97
w/ glass	5.3	4.1	1.8	0.91

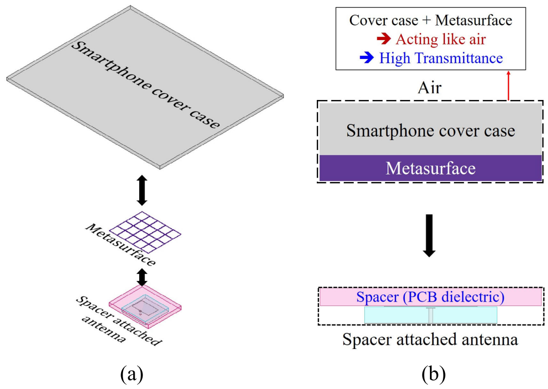

Fig. 3. Concept map of MCA. (a) Overall view. (b) Side view.

means that the beam coverage of the antenna is deteriorated by the glass. We believe that the transmittance of Gorilla Glass at 28 GHz is significantly poorer than that of air. Increasing the transmittance by changing the thickness or physical properties of the cover case would make performance degradation less likely; however, it is difficult to change the thickness and physical properties of the commercial smartphone cover case. Therefore, in Section II-B, we discuss a method to improve the transmittance by inserting a thin metasurface under the cover case without changing the cover case.

B. Gain Enhancement Principle and Metasurface Design

Fig. 3 shows a concept map illustrating the principle of improving antenna radiation performance by bonding a metasurface below the cover case, which is the proposed MCA. The cover case is the main factor that deteriorates antenna performance, but when combined with the metasurface, it can operate with an aperture larger than the patch size, leading to improved radiation performance of the antenna. To improve the radiation performance of the antenna, the metasurface combined with the cover case must have better transmittance in the target frequency than the cover case. In Fig. 2, the reason why the radiation performance of the antenna covered by the cover case is not good is because the transmittance of the cover case is worse than that of air. The concept of MCA presented in Fig. 3 is to reduce the radiation performance degradation by combining the cover case, which reduces radiation performance, with a metasurface to have a transmittance similar to that of air. In this study, since the metasurface was designed using a general PCB process, a PCB dielectric is inevitably placed as a spacer on the antenna aperture, as shown in Fig. 3(b). Since it is difficult to control the distance between the aperture and the metasurface in actual measurement, attaching this spacer on the top of the aperture can physically keep the distance between the aperture and the metasurface constant. Then, on the top of this spacer, a cover case or a metasurface, such as ILM or Capacitively loaded metasurface (CLM), is attached.

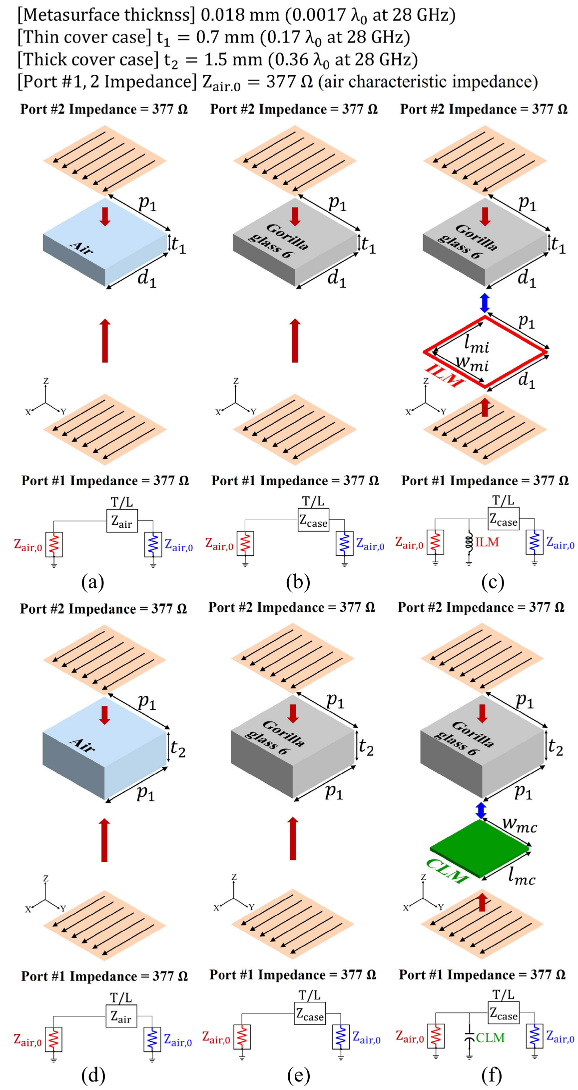

Fig. 4. Illustrations of floquet two-port simulation of unit cell model applying far-field region conditions. (a) Thin air model (reference). (b) DS with the thin cover-cased model. (c) ILM with thin cover-cased model. (d) Thick air model (reference). (e) DS with the thick cover-cased model. (f) CLM with thick cover-cased model.

TABLE II
DESIGN PARAMETERS AND THEIR VALUES OF STRUCTURES IN FIG. 4 (ALL PHYSICAL DIMENSIONS ARE IN mm)

d_1	2	l_{mi}	1.9	l_{mc}	1.2
p_1	1.9	w_{mi}	1.8	w_{mc}	1.2
t_1	0.7	t_2	1.5		

Fig. 4 shows the structure of the floquet two-port simulation to which the cover case and metasurface are applied. The impedance of both ports is set to 377 Ω, the characteristic impedance of air. In this study, in order to make the transmittance of the cover case combined with the metasurface as close as possible to air, the metasurface was designed to have response characteristics similar to air under two conditions.

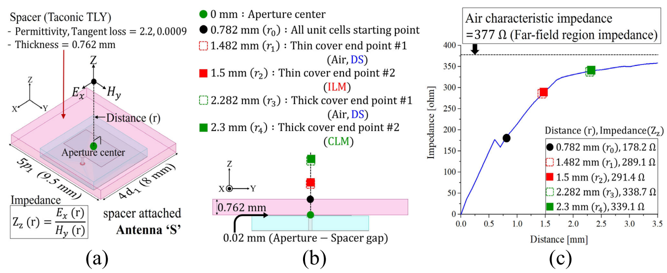

Fig. 5. Spacer attached antenna near-field impedance derivation conceptual diagram. (a) Over all. (b) Side view. (c) Impedance graph.

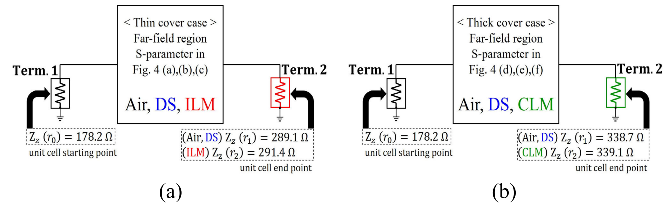

Fig. 6. Simulation diagram applying near-field impedance and far-field S-parameters. (a) Thin cover case application. (b) Thick cover case application.

First, through the floquet simulation in Fig. 4, the response characteristics of the metasurface can be similar to that of air in the far-field region. This is one of the commonly applied methods of designing a transmit array. In Fig. 4(a) and (d), the thickness of the air was made the same as the thickness of the cover case applied. The name of the unit cell was determined based on the material that is combined under the cover case in the antenna. In the case of Fig. 4(b) and (e), the dielectric spacer is combined right below this cover case, so it was named as "DS." Also, since both port impedances are set to the characteristic impedance of air, the transmittance in Fig. 4(a) and (d) becomes 0 dB. The first starting point for metasurface design is to bring the transmittance of the structure combining metasurface and cover case as close as possible to this reference through floquet two-port simulation. The second metasurface design condition is to have a value similar to air when the S-parameter obtained by applying the far-field condition in Fig. 4 is terminated with the antenna near-field impedance. If both the far-field and near-field show the same transmittance response results as air, the ideal design conditions are satisfied. In this study, the metasurface was designed by setting these two conditions as references.

The antenna in Fig. 5(a) shows the structure of the antenna "S" with a spacer attached. Antenna "S" is a conventional patch antenna designed to resonate at 28 GHz and radiate x-polarized signals. The spacer used is a Taconic TLY, and the thickness is 0.762 mm, and the area is 9.5 mm wide (y-axis) and 8 mm long (x-axis), and it is an area that can be placed as many as five units horizontally and four units vertically. In order for the floquet simulation result of Fig. 4 to be effective, it was designed to occupy a larger area by half a wavelength horizontally and vertically than the antenna aperture. Next, the meaning of the distance from the center of the aperture of antenna "S" is shown in Fig. 5(b). Antenna "S" can be thought of as having air unit cells with a thickness of 0.7 or 1.5 mm placed in the point marked with a black circle. The red dotted line box filled with white is the endpoint of the DS unit cell in Fig. 4(b), which consists of only a thin cover case without a metasurface. Also, the red box is the endpoint of the ILM unit cell in Fig. 4(c), where the ILM and thin cover case are combined. Next, the result of obtaining the antenna impedance according to the distance from the center of the aperture of antenna "S" is shown in Fig. 5(c). Antenna "S" is an antenna that operates with X-polarization, so the dominant electrical field component is E_x. Therefore, the impedance at a point away from the aperture by a distance "r" in the vertical direction is as follows:

$$Z_z(r) = E_x(r)/H_y(r). \tag{1}$$

The impedance at the point in Fig. 5(b) is shown in Fig. 5(c), and it can be seen whether the second design condition is satisfied from the transmittance obtained by setting these impedances to both terminations. If the response characteristics of the unit cell where the cover case and metasurface are combined are ideally equal to air, the two-port S-parameter result of the far-field area shown in Fig. 4 will be the same as that of the air unit cell. Furthermore, even if both sides of this S-parameter are terminated with the impedance of the starting point shown in Fig. 5(c), and the endpoint that is the same distance away from this starting point, the result will be the same as air. The key to this study is to design a metasurface that shows the response characteristics similar to air in both the far-field and near-field regions according to this ideal condition. If the designed metasurface has the response characteristics similar to air even under the far-field and near-field conditions, it will appear as air when applied to an actual antenna. Accordingly, reflection due to the cover case can be reduced, and thus, the beam coverage in the main radiation direction will be improved. A conceptual diagram of the second design condition is shown in Fig. 6. The starting point of all unit cells shown in Fig. 4 is a black circle, and its impedance is 178.2 Ω. Therefore, in all cases, set the port impedance on one side to this 178.2 Ω. When applying a thin cover case, the thickness of the air and cover case in Fig. 4(a) is 0.7 mm. Therefore, the impedance at 1.482 mm away from the starting point by 0.7 mm was designated as the remaining port impedance of air and DS. However, since the thickness of the ILM unit cell in Fig. 4(c) combined with the cover case is 0.718 mm, the impedance at 1.5 mm is set as the port impedance. Also, when a thick cover case was applied, the port impedance should be set according to the thickness. Figs. 7 and 8 show the simulation results of the response characteristics of the metasurface designed according to the two conditions mentioned above. Fig. 7 shows the simulation result when both port impedances are set to 377 Ω, the characteristic impedance of air, according to the conditions of the far-field area, and Fig. 8 shows the simulation result applying the impedance in the near-field area. The black dotted lines in Figs. 7 and 8 are the results when the air unit cells presented in Fig. 4(a) and (d) are applied, and serve as a design reference.

The simulation results of the DS indicated by the blue lines in Figs. 7 and 8 are the unit cell simulation results with only the cover case and no metasurface applied, and the unit cell

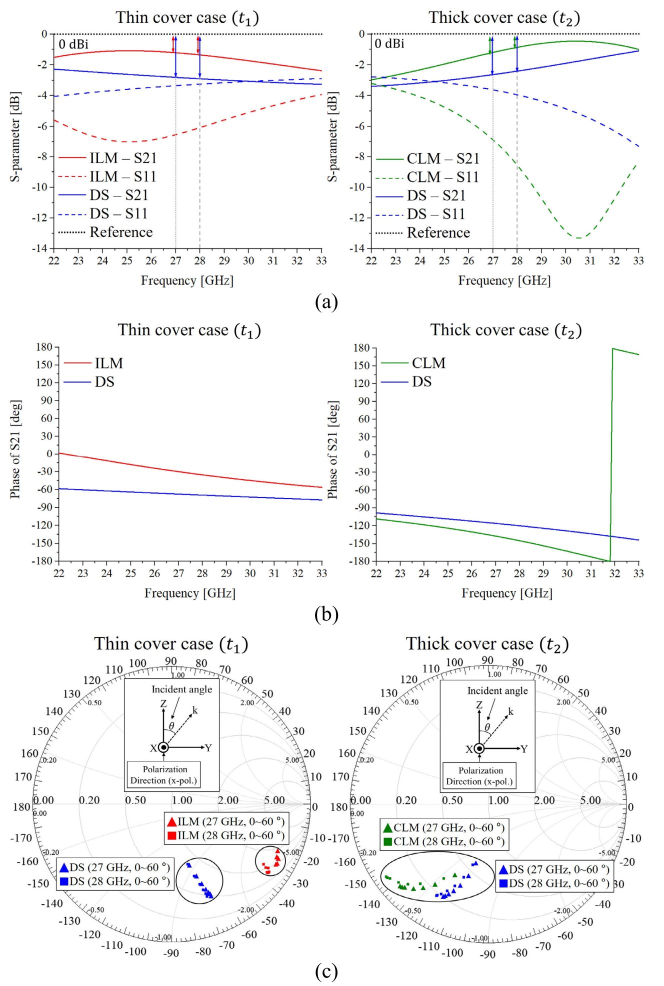

Fig. 7. Simulation results of the floquet two-port network applying far-field region conditions. (a) Magnitude of S-parameters. (b) Phase of S_{21}. (c) Smith chart (S_{21}) of unit cells according to incident angle change.

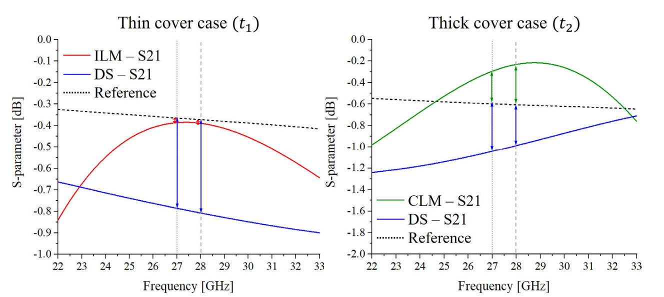

Fig. 8. Simulation results of two-port network applying near-field impedance and far-field S-parameters.

structure corresponds to Fig. 4(b) and (d). The simulation result indicated by the red line corresponds to the case, where the ILM is attached under the thin cover case and is shown in Fig. 4(c). As can be seen from Figs. 7(a) and 8, when this ILM is attached under the cover case, the transmittance difference with the reference (air unit cell) becomes smaller than DS. Therefore, it can be concluded that the structure combining this ILM under the cover case operates more similar to air than the case where there is only a cover case. Similarly, in the case of CLM with a thick cover case, the difference

TABLE III

DIFFERENCE IN TRANSMITTANCE FROM REFERENCE IN FIGS. 7 AND 8

Types of unit cell model	Frequency : 27 GHz		Frequency : 28 GHz	
	(Far-field) Difference of S_{21} (dB)	(Near-field) Difference of S_{21} (dB)	(Far-field) Difference of S_{21} (dB)	(Near-field) Difference of S_{21} (dB)
ILM (thin)	1.20	0.0216	1.36	0.0169
DS (thin)	2.81	0.426	2.90	0.441
CLM (thick)	1.18	0.304	0.85	0.375
DS (thick)	2.63	0.447	2.40	0.384

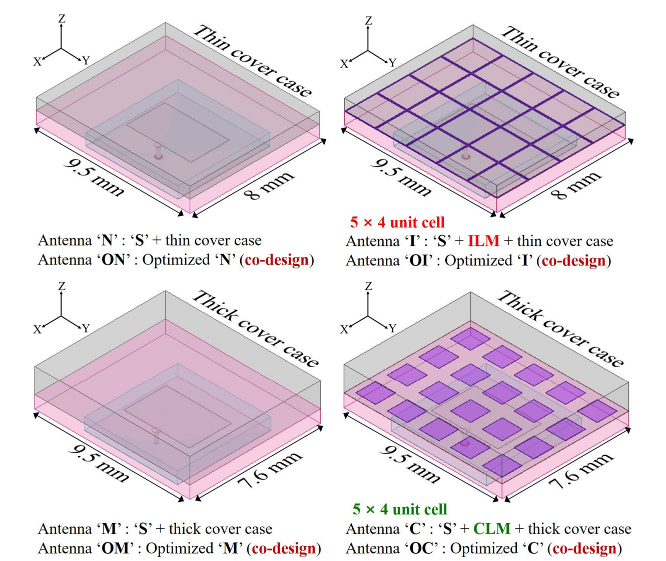

Fig. 9. Antenna structural diagram with metasurface and cover case applied.

in transmittance with the reference is smaller than that with DS, and it can be seen that it operates more similar to air. Table III summarizes the transmittance difference from the reference at 27 and 28 GHz, and it can be seen that both the ILM with a thin cover case and the CLM with a thick cover case are designed closer to the reference than the DS with only a cover case. Fig. 7(c) shows the transmittance trajectory when the incident angle is changed in the far-field area as a Smith chart, and the outermost circle shows the trajectory of the air unit cell. Therefore, even if the incident angle changes, if the transmittance changes close to this outermost trajectory, it can be seen that the transmittance does not change significantly according to the incident angle. It can be seen that both ILM and CLM are closer to the trajectory of air than DS.

Fig. 9 shows the structure of the metasurface designed through this process and the analysis applied to the antenna. There are a total of nine types of single antennas, including the antenna "S" in Fig. 5 mentioned above. Antenna "S" is a case where an air unit cell is attached to a spacer without a cover case and is an antenna to which the air unit cell in Fig. 4 is applied as a reference. Therefore, if the metasurface ideally changes the cover case to air, it will perform the same operation as this antenna "S," so the performance of this antenna "S" can be used as a reference. Antenna "N" is a case in which a thin cover case is combined with antenna "S," and the antenna "ON" has a resonance frequency at 28 GHz through co-design that optimizes the antenna structure while

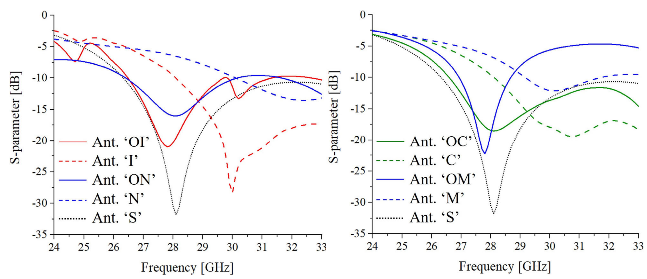

Fig. 10. S-parameter results (S_{11}) of nine types of antennas.

combining the thin cover case and antenna. In the same way, antenna "I" is a case where ILM and thin cover case are combined with antenna "S," and the antenna "OI" is an antenna structure optimized to resonate at 28 GHz by co-designing this. In order to see the improvement in antenna radiation performance by ILM when a thin cover case is applied, the performance of the antenna "ON" and the antenna "OI" can be compared. The description of the antennas to which the thick cover case is applied is also shown in Fig. 9, and to check the radiation performance improvement by CLM, the performance of the antenna "OM" and the antenna "OC" s should be compared.

Fig. 10 shows a graph showing the reflection coefficients of nine types of antennas. If the designed metasurface is combined with the thin cover case and ideally operates like air, and there is no coupling with the aperture, there will be no shift in resonance frequency even when combined with the antenna "S." Comparing the reflection coefficient performance of antenna "S" and antenna "I," it can be seen that the resonant frequency shifted by about 2 GHz. This is due to the difference in response characteristics between references in the far field and near field. However, in the case of DS without ILM, a larger resonant frequency shift occurred around 4 GHz, and the reflection coefficient at 28 GHz was not good when compared with "I." This is because a lot of reflection occurred in the cover case because the difference in response characteristics of the DS unit cell was large when compared with the reference. As a result, the antenna impedance is changed in the near-field area, and the matching is more distorted than when ILM is applied. When the thick cover case was applied, the reflection coefficient characteristics at 28 GHz of the antenna "C" to which the CLM was applied were better than that of "M" to which only the cover case was applied, but the difference in resonance frequency did not occur significantly. This is because the coupling with the antenna aperture, which occurs when CLM is applied to an actual antenna, is not reflected in the metasurface design. Previously, in the case of ILM, the grid structure was designed to have a very thin line thickness, so the coupling with the aperture could be ignored. This affects antenna matching and thus affects the reflection coefficient. Therefore, when designing a metasurface, it is more advantageous to design a metasurface with a structure that minimizes coupling with the aperture, such as ILM. Fig. 11 shows a graph showing antenna radiation patterns in the H-plane at 27 and 28 GHz. The radiation pattern of antenna "S," which radiates signals from the top of the spacer to free space without a cover case, is indicated by a black dotted line. Previously, it was expected that a large reflection would occur in the cover case because the unit cell response characteristics of the DS combined with the thin cover case on the antenna "S" had a large difference from the reference. It can be seen from Fig. 11(a) that the prediction was correct. As indicated by the blue dotted line, when the cover case is coupled to the antenna "S," it can be seen that a lot of back radiation is generated by this cover case. Also, even if the antenna structure is optimized through co-design, and the maximum signal is radiated at 28 GHz, it can be seen from the blue solid line that all reflections caused by the cover case cannot be canceled out. On the other hand, if an ILM with unit cell response characteristics similar to the reference and structurally less coupling with the aperture is inserted under the thin cover case, something very surprising happens. Looking at the radiation pattern results of "I" and "N" indicated by red and blue dotted lines, respectively, it can be seen that the back radiation is significantly reduced just by inserting an 18-μm-thick metasurface under the thin cover case. Since the back radiation is drastically reduced, the radiation performance in the main radiation direction including the bore sight is improved. Furthermore, by changing the structure of the antenna to radiate the maximum signal at 28 GHz through co-design, it is possible to design an antenna close to the radiation performance of the reference antenna "S." This can be seen by comparing the radiation pattern performances of the black dotted line and the red solid line. In the case of CLM designed by applying a thick cover case, the performance improvement was lower than that of ILM. First of all, this is a result because the response characteristics of the CLM unit cell were not as close to the reference as the ILM unit cell, and the coupling effect between the aperture and the CLM was not reflected in the design of the metasurface. Reflecting the coupling problem between the aperture and the metasurface from the design stage remains a task for future research.

Section III shows the antenna design and radiation performance results when the metasurface area is increased and a cover case with a large area like a commercial smartphone is applied. At this time, the performance of all antennas was compared with the state of co-design.

III. Metasurface-Cased Antenna Design

The flowchart of the method for designing the metasurface is schematized in Fig. 12. First, the material type and thickness of the smartphone cover case were selected. This is crucial because the pattern of the metasurface depends on the characteristics of the cover case. Second, a floquet two-port network simulation and near-field impedance applying simulation were performed by combining the selected cover case and the designed metasurface. By comparing the S_{21} results of various metasurfaces combined with a cover case, a suitable structure was selected to improve the antenna beam performance. As previously mentioned in Section II, the beam coverage performance of the antenna deteriorated owing to the poor transmittance of the cover case in the target frequency band. Therefore, the metasurface attached to the

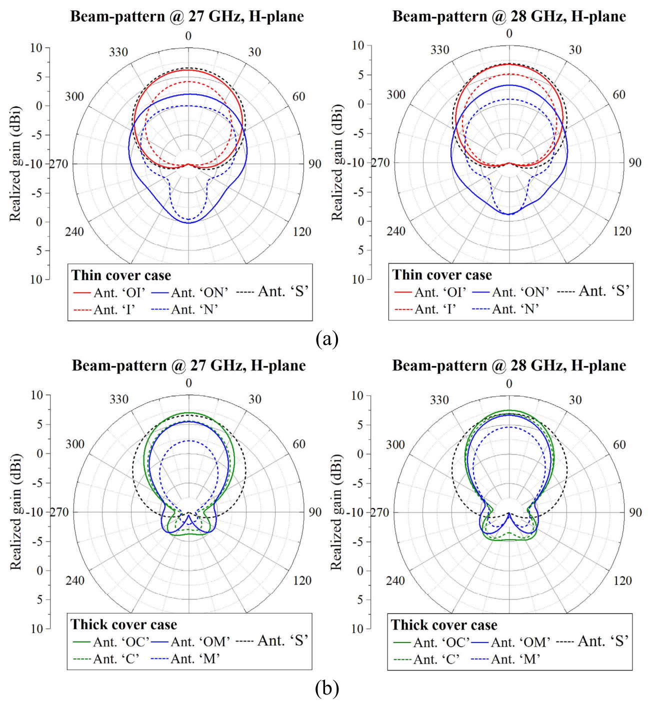

Fig. 11. Simulated radiation patterns of nine types of antennas. (a) Thin cover case application. (b) Thick cover case application.

TABLE IV
COMPARISON OF NINE TYPES OF ANTENNA P.G

Frequency	Peak gain (dBi) [Thin cover case applied Ant.]					Peak gain (dBi) [Thick cover case applied Ant.]				
	S	OI	I	ON	N	S	OC	C	OM	M
27 GHz	6.5	6.3	4.3	2.4	1.5	6.5	7.2	6.1	5.5	2.7
28 GHz	6.9	6.8	5.2	3.6	2.1	6.9	7.7	7.4	7.0	4.7

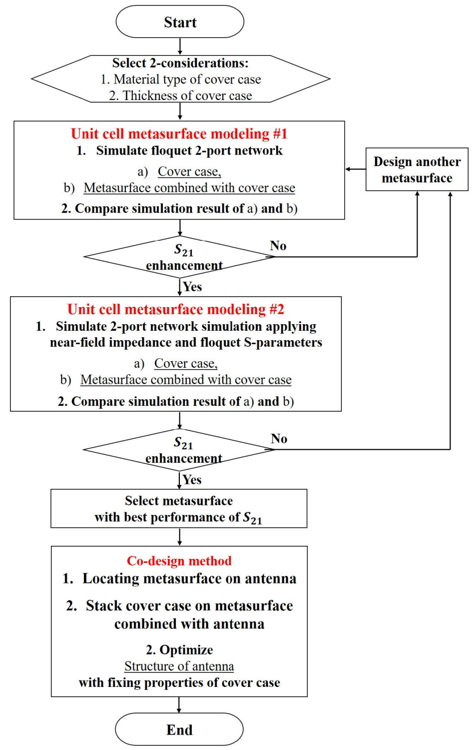

Fig. 12. Method flowchart on the unit cell modeling of a metasurface and co-design method of a smartphone antenna.

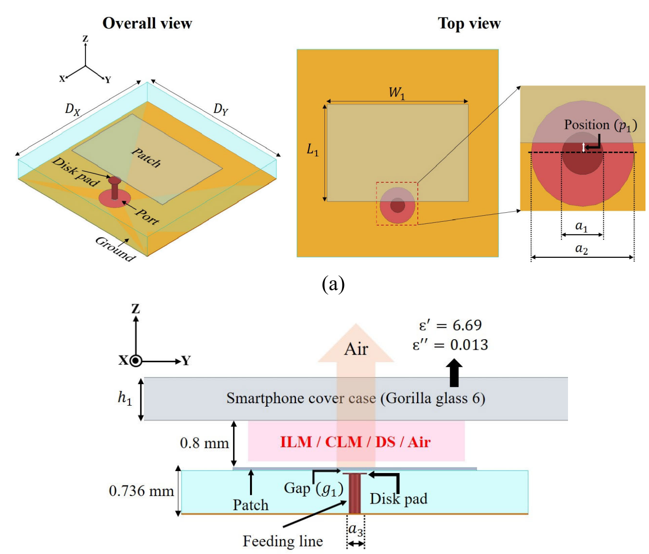

Fig. 13. Structural diagram of single antenna applied with metasurface. (a) Overall and top view of the antenna. (b) Side view of the antenna with a metasurface.

TABLE V
DESIGN PARAMETERS AND THEIR VALUES OF STRUCTURES IN FIG. 13 (ALL PHYSICAL DIMENSIONS ARE IN mm)

D_X	5.7	W_1	4	a_1	0.36	g_1	0.4
D_Y	5.7	h_1	0.7 / 1.5	a_3	0.2		

cover case can enhance the beam performance by increasing the transmittance. Optimizing the impedance matching and radiation pattern while combining the antenna, metasurface, and cover case is the final step (co-design). The detailed metasurface modeling process used is presented in Figs. 3–8.

The metasurface applied to the antenna in this study is different from that used for lenses or superstrates covered in many other papers [11], [12], [14], [15], [16], [17], [18], [19], [20], [21], [22]. This is because the metasurface used as a lens operates far away from the antenna. In contrast, the metasurface proposed in this study is directly connected to the antenna and operates as a resonator while mounted on the smartphone to increase the gain.

A. Single-Cased Antenna

To verify the prediction stated above, the radiation performance of various single-cased antennas developed through co-design should be comparatively analyzed. The structure of all antennas to be covered in Section III is shown in Fig. 13. The values fllisted in Table V are fixed values, and other parameters are changed to optimize performance during co-design. As shown in Fig. 13(b), the distance between the antenna and the cover case is fixed at 0.8 mm, and a metasurface or dielectric is inserted into this space. The proposed single-cased antenna containing a metasurface and a cover case is shown in Fig. 14. The applied unit cell-cased

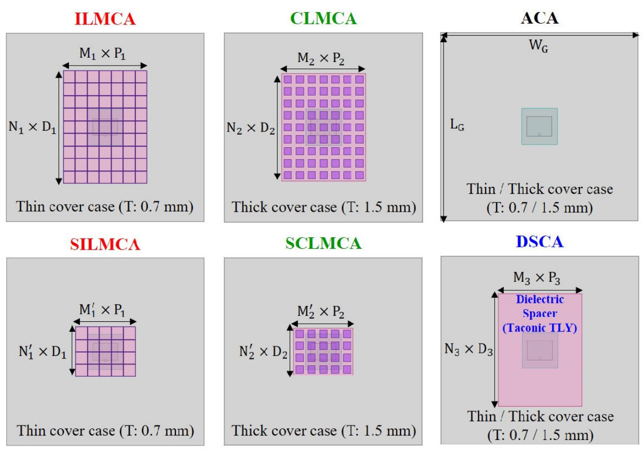

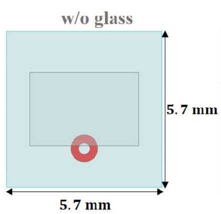

P_1 (mm)	1.9	D_1 (mm)	2	M_1 (#)	7	N_1 (#)	9	M_1' (#)	5	N_1' (#)	4
P_2 (mm)	1.9	D_2 (mm)	1.9	M_2 (#)	7	N_2 (#)	9	M_2' (#)	5	N_2' (#)	4
P_3 (mm)	1.9	D_3 (mm)	2 / 1.9	M_3 (#)	7	N_3 (#)	9	L_G (mm)	30	W_G (mm)	37.2

- Conventional patch antenna
- Direct radiation w/o glass

Fig. 14. Illustration of single-cased antennas.

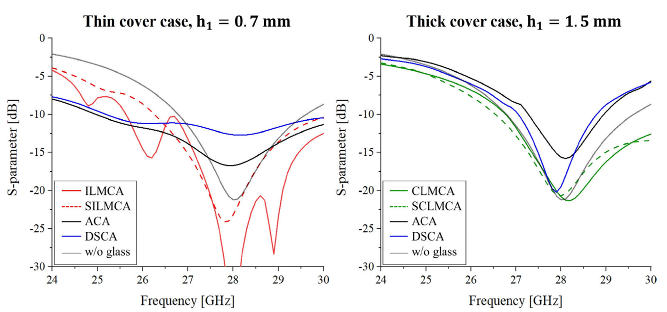

Fig. 15. S-parameter results (S_{11}) of the single-cased antennas.

models are air, DS, ILM, and CLM structures covered in Section II-B. In Section II-B, we established that the ILM improves the transmittance in the case of a thin cover case (0.7 mm), and the CLM improves the transmittance in the case of a thick cover case (1.5 mm). To verify the beam coverage improvement by the metasurface, in the thin cover case, the performance of the antenna applied with the ILM-cased model was compared with that of the antenna applied with the DS and air-cased model. For the thick cover case, the antenna to which the CLM-cased model was applied was compared with the antenna to which DS and air-cased models were applied. For convenience, the single-cased antennas in Fig. 14 are named as ILMCA, small-IMCA (SILMCA), capacitively loaded MCA (CLMCA), small-CLMCA (SCLMCA), DSCA, and air-cased antenna (ACA). During co-design, the structure of the antenna should be optimized. Fig. 15 shows an S_{11} graph showing that the antennas resonate at 28 GHz through the metasurface and antenna co-design. All the antennas to be discussed in Section III are thus optimized to resonate at 28 GHz.

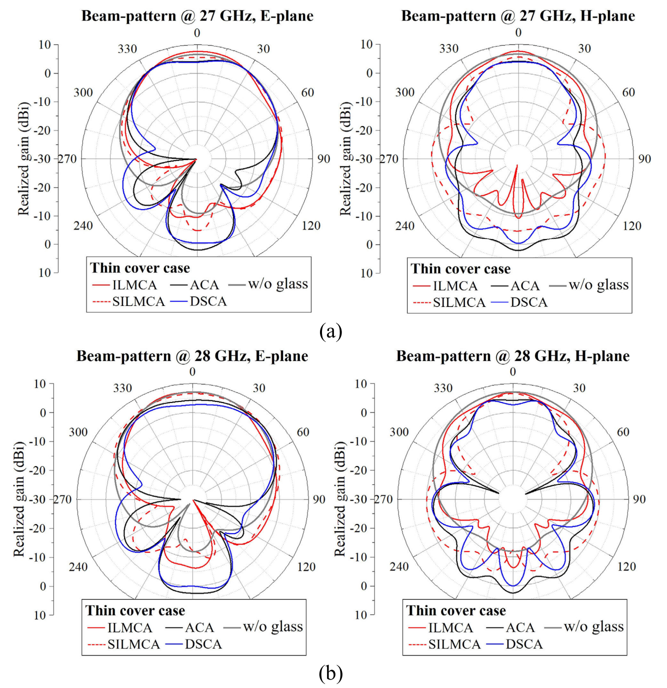

Fig. 16. Simulated radiation patterns of the single-cased antennas with a thin cover case (thickness = 0.7 mm) and single antenna without glass. (a) 27 GHz. (b) 28 GHz.

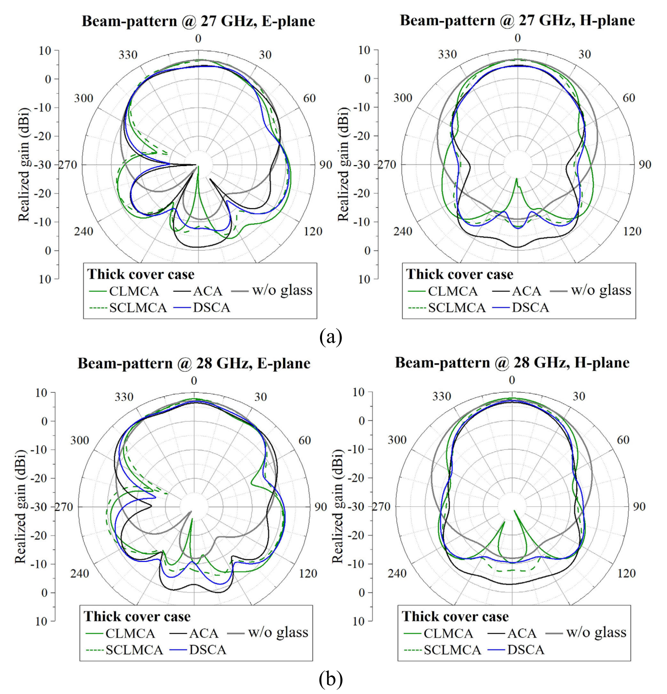

Fig. 17. Simulated radiation patterns of the single-cased antennas with a thick cover case (thickness = 1.5 mm) and single antenna without glass. (a) 27 GHz. (b) 28 GHz.

Figs. 16 and 17 and Tables VI and VII present the radiation patterns, realized gain, and total efficiency of single-cased antennas and single antenna that radiates directly into the air without a cover case (referred to as a "w/o glass"). As comparing the beam coverage performance with only the radiation pattern is difficult, P.G, T.Q.G, M.G, and total

TABLE VI
GAINS OF THIN COVER CASE APPLIED ANTENNAS

Types of antennas	Frequency : 27 GHz				Frequency : 28 GHz			
	P.G (dBi)	T.Q.G (dBi)	M.G (dBi)	Total Eff.	P.G (dBi)	T.Q.G (dBi)	M.G (dBi)	Total Eff.
ILMCA	7.7	4.7	1.9	0.84	7.1	4.8	1.8	0.9
SILMCA	6.1	3.7	2.2	0.89	6.6	4.5	2.7	0.94
ACA	5.9	3.7	1.4	0.85	5.3	4.1	1.8	0.91
DSCA	5.8	3.6	1.1	0.88	5.0	3.0	0.9	0.87
w/o glass	6.6	5.7	3.3	0.95	7.1	6.2	3.7	0.97

TABLE VII
GAINS OF THICK COVER CASE APPLIED ANTENNAS

Types of antennas	Frequency : 27 GHz				Frequency : 28 GHz			
	P.G (dBi)	T.Q.G (dBi)	M.G (dBi)	Total Eff.	P.G (dBi)	T.Q.G (dBi)	M.G (dBi)	Total Eff.
CLMCA	6.8	4.6	2.1	0.85	7.8	5.6	3.0	0.91
SCLMCA	6.6	4.9	2.2	0.88	7.5	5.4	2.7	0.92
ACA	4.9	3.1	1.4	0.81	6.4	4.3	2.5	0.9
DSCA	5.0	3.2	1.0	0.92	6.9	4.7	2.6	0.89
w/o glass	6.6	5.7	3.3	0.95	7.1	6.2	3.7	0.97

efficiency shown in Tables VI and VII should be analyzed. When comparing the gain performance of the antennas with the cover case applied, it can be observed that the ILM and CLM perform excellently when the metasurface is applied. The result of applying the metasurface to the array antenna will be analyzed in Section III-B, as the beam coverage is improved when the metasurface is applied to a single antenna.

B. 1 × 4 Array-Cased Antenna

Fig. 18 shows the structure when the metasurface is applied to the array antenna. The spacing between the array antenna elements is 5.7 mm, and the overall size is 5.7 × 22.8 mm. The number of metasurface unit cells is 9 in the polarization direction and 16 in the array direction. When a thin cover case was applied, the unit cell length in the polarization direction of the DS was set to 2 mm to apply the same area as the ILM area. Similarly, when the thick cover case was applied, it was set to 1.9 mm to match the metasurface area of the CLM. Here, the array antenna beam coverage superiority or inferiority is determined by comparing the beam steering performance of the array antennas. This involves comparing the value of the steered gain when the phase difference between each element is applied at 0°, 45°, 90°, and 135°. The comparison of beam steering simulation results is detailed in Fig. 19 and Table VIII. Fig. 19(a) and (b) shows the beam steering performance when thin and thick cover cases are applied, respectively.

Comparing the values listed in Table VIII, it can be observed that the beam steering performance of the antennas to which the previously designed ILM and CLM are applied is significantly superior. For example, the gain in the boresight direction of ILMCA with a thin cover is 11.7 and 12.2 dBi at 27 and 28 GHz, respectively. These values are very similar to the boresight gain (11.6 and 12.2 dBi) of a conventional antenna (“w/o glass”) to which no cover case is applied. This tendency is maintained even when a phase difference

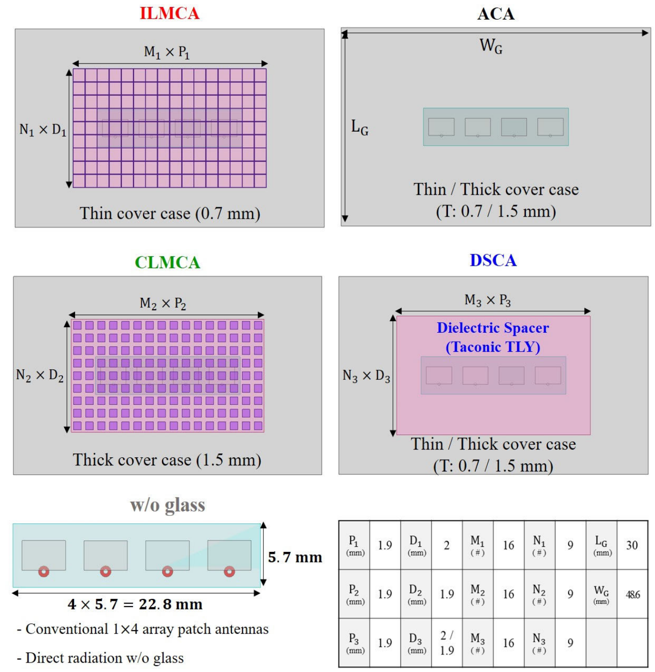

Fig. 18. Illustration of the 1 ×4 array-cased antennas.

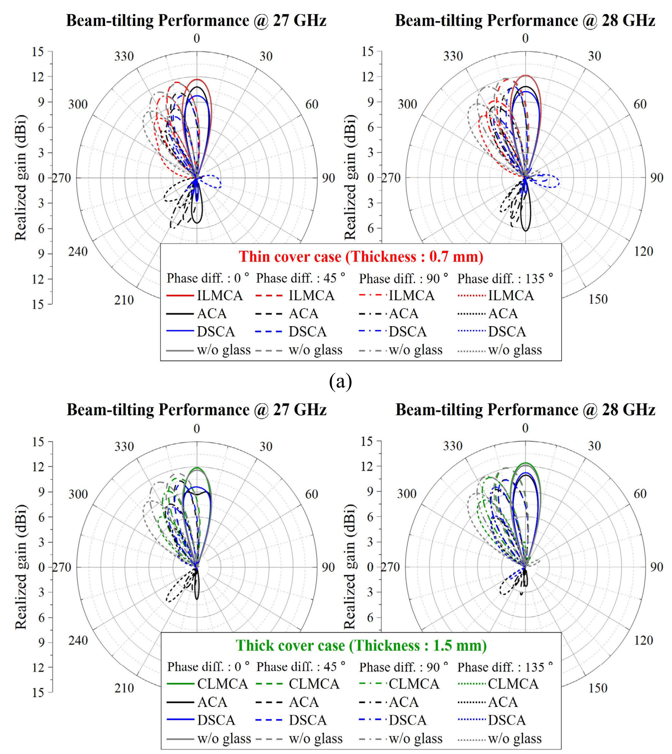

Fig. 19. Simulated beam tilting performances of the 1 × 4 array-case antenna in the *YZ* plane at 27 and 28 GHz. (a) Thin and (b) thick cover cases applications.

of 45° is given between each element of the antenna. The gain when the beam is steered by approximately 13° owing to the phase difference of 45° is 11.6 and 11.9 dBi at 27 and 28 GHz, respectively, which is similar to that of the w/o glass. Conversely, when the phase difference between elements

TABLE VIII
SUMMARIZED SIMULATED BEAM TILTING PERFORMANCES (P.G/TILTING DEGREE) OF FIG. 19 AT 27 AND 28 GHz

(a)

Phase diff. (°)	ILMCA (dBi / °)	ACA (dBi / °)	DSCA (dBi / °)	w/o glass (dBi / °)
0	11.7 / 0	10.8 / 0	9.7 / 0	11.6 / 0
45	11.6 / 13	10.3 / 13	9.9 / 12	11.5 / 13
90	10.6 / 24	8.7 / 20	7.9 / 25	11.3 / 27
135	8.6 / 36	7.1 / 38	4.7 / 37	9.9 / 39

(b)

Phase diff. (°)	ILMCA (dBi / °)	ACA (dBi / °)	DSCA (dBi / °)	w/o glass (dBi / °)
0	12.2 / 0	10.8 / 0	10.2 / 0	12.2 / 0
45	11.9 / 13	10.7 / 11	11.0 / 9	12.0 / 14
90	10.0 / 26	9.3 / 27	8.1 / 28	11.9 / 27
135	9.2 / 37	6.6 / 36	3.5 / 34	10.9 / 38

(c)

Phase diff. (°)	CLMCA (dBi / °)	ACA (dBi / °)	DSCA (dBi / °)	w/o glass (dBi / °)
0	11.9 / 0	8.7 / 0	9.6 / 0	11.6 / 0
45	11.0 / 14	10.5 / 12	10.1 / 12	11.5 / 14
90	9.8 / 23	8.3 / 26	8.0 / 24	11.3 / 27
135	7.6 / 38	5.5 / 33	4.6 / 33	10.0 / 39

(d)

Phase diff. (°)	CLMCA (dBi / °)	ACA (dBi / °)	DSCA (dBi / °)	w/o glass (dBi / °)
0	12.4 / 0	10.9 / 0	11.2 / 0	12.1 / 0
45	12.0 / 13	10.7 / 14	10.7 / 14	12.0 / 14
90	11.6 / 24	9.9 / 23	10.2 / 23	11.9 / 27
135	9.6 / 36	7.1 / 35	7.3 / 35	10.9 / 38

TABLE IX
SUMMARIZED SIMULATED BEAM TILTING PERFORMANCES (P.G/TILTING DEGREE) OF FIG. 21 AT 27 AND 28 GHz

(a)

Phase diff. (°)	ILMCA peak gain / tilting degree (dBi / °)	DSCA peak gain / tilting degree (dBi / °)	w/o glass peak gain / tilting degree (dBi / °)
0	11.63 / 0	10.94 / 0	11.88 / 0
45	12.23 / 14	10.22 / 10	11.87 / 13
90	10.94 / 24	7.29 / 23	11.52 / 25
135	9.75 / 35	3.25 / 35	10.04 / 38

(b)

Phase diff. (°)	ILMCA peak gain / tilting degree (dBi / °)	DSCA peak gain / tilting degree (dBi / °)	w/o glass peak gain / tilting degree (dBi / °)
0	12.6 / 0	11.42 / 0	11.84 / 0
45	10.87/ 12	10.29 / 10	11.88 / 13
90	10.31 / 25	7.19 / 24	11.64 / 26
135	7.91 / 35	2.93 / 43	10.06 / 38

increases, the gain value decreases compared with the case where there is no cover case. However, Fig. 19 and Table VIII show that the deterioration of the beam steering performance compared with that of w/o glass as the steering angle is changed is significantly smaller than that of the ACA and DSCA without a metasurface. This is because the reduction of the beam coverage performance by the smartphone cover case is mitigated through the metasurface. Similarly, when the thick cover case is applied, the boresight gains of the CLM are greater than that of the ACA and DSCA, and the degree of performance degradation according to the steering angle is less than that of the ACA and DSCA.

TABLE X
SUMMARIZED SIMULATED BEAM TILTING PERFORMANCES (P.G/TILTING DEGREE) OF FIG. 24

Phase diff. (°)	ILMCAiP (dBi / °)	DSCAiP (dBi / °)
0	9.01 / 0	8.25 / 0
45	9.74 / 15	8.32 / 16
90	9.62 / 24	3.35 / 22
135	6.54 / 33	-3.21 / 90

TABLE XI
SUMMARIZED MEASURED BEAM TILTING PERFORMANCES (NORMALIZED GAIN/TILTING DEGREE) OF FIG. 30

Phase diff. (°)	ILMCAiP (dB / °)	DSCAiP (dB / °)
0	0 / 0	-4.58 / 0
45	-0.72 / 12	-4.99 / 12
90	-3.22 / 27	- 7.54 / 30
135	-2.7 / 3	- 7.83 / 3

IV. WHOLE CONFIGURATION OF A 1 × 4 ARRAY METASURFACE-CASED ANTENNA

A suitable unit cell metasurface for beam-coverage enhancement has been designed by changing the thickness of the cover case in Sections II and III. However, here, the thickness of the cover case is fixed at 0.7 mm, and only the thin cover case is used. This is because the thickness of a real smartphone cover glass is approximately 0.7 mm. In Sections II and III, ILMCA is the antenna with the best radiation performance when a thin cover case with a thickness of 0.7 mm was placed on the antenna. Therefore, here, the 1 × 4 array ILMCA and DSCA are designed, and their performance is compared to determine whether the beam coverage of the antenna is improved by the ILM.

A. Design of Array MCA

Fig. 20 shows the overall structure of the array ILMCA. The cover case is applied with Corning Gorilla Glass 6, and the metasurface is designed as a Taconic TLY substrate with a small dielectric constant and loss. The area of the metasurface is 34 × 22 mm, with a thickness of 0.78 mm, and the thickness combined with the antenna is 1.63 mm. As the combined thickness of the metasurface and the antenna is less than 2 mm, it can be considered sufficiently thin to be mounted on a commercial smartphone. The Gorilla Glass 6, with a thickness of 0.7 mm, is used to verify the practicality of the topology proposed in this article, similar to the single-cased antenna. The area of this cover case is 48.6 × 30 mm, which is sufficiently large compared with the antennas. As shown in the figure, after combining the array antenna, ILM, and cover case, co-design is performed to optimize the antenna performance. As mentioned earlier, this array antenna has high compatibility because the performance is optimized by considering the metasurface and the cover case, and the metasurface is under the cover case so that the metasurface is not exposed to the

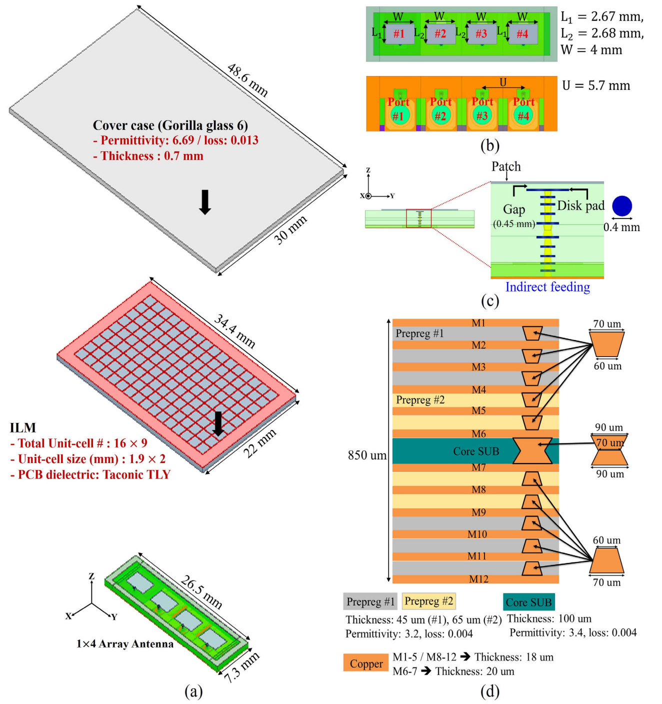

Fig. 20. Configuration diagram of the production version of the 1 × 4 array ILMCA. (a) Overall view, (b) top and rear views, (c) indirect feeding method, and (d) PCB stack-up structure.

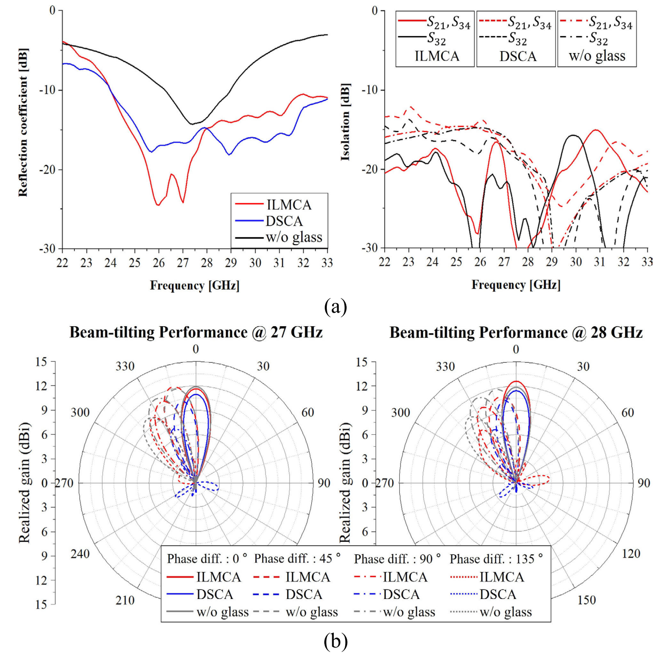

Fig. 21. Simulated results of the production version of the 1 × 4 array-case antenna. (a) Reflection coefficient and isolation. (b) Beam tilting performances in the *YZ* plane at 27 and 28 GHz.

outside; therefore, it is practical in terms of packaging. The metasurface proposed in this way has a different topology from a superstrate that cannot be mounted on a smartphone by thick designing without considering the cover case, and a lens that operates far away from the antenna. A detailed depiction of the 1 × 4 array antenna structure is shown in Fig. 20(a)–(d). As shown in the figure, the thickness of the 1 × 4 array antenna is 0.85 mm, the dimension size is 26.5 × 7.3 mm, and the distance between elements is 5.7 mm. There is a pad for soldering mini SMP on the back of the antenna in Fig. 20(c), and the simulation was executed by inputting the mini SMP CAD information provided by the connector manufacturer.

The simulation results of the antenna beam tilting performance through phase change after attaching four-mini SMPs to the rear of the antenna are presented in Section IV-B. Antenna feeding was given as a disk indirect with the patch using PCB stack-up technology. The resonance point and bandwidth of the antenna can be controlled by the size of the patch and the diameter and position of the disk. In addition, a symmetry structure was applied to this array antenna. As the center point of the array antenna is symmetrical, all structures of 1 and 4, and 2 and 3 have the same size. By using this, the array antennas could be easily optimized.

Fig. 20(d) shows the PCB stack-up structure used widely to produce 5G smartphone antennas, and the antennas in this study were made using this technology. The technology is used to extend the degree of freedom for designing an antenna. The structure has 12 layers with a height of 850 μm, as shown in Fig. 20(d). To increase stability, a chain of via holes in multilayers of a via-hole shape was designed as trapezoids for alignment. Various techniques for improving the performance of the antenna could be easily applied using this technology. As illustrated in Fig. 20(c), an indirect feeding method can be used to widen the bandwidth of the antenna [9].

B. Simulation Results

The simulation results of two types of array-cased antennas (ILMCA and DSCA) and an array antenna without cover case (w/o glass) are presented in Fig. 21 and Table IX. Red, blue, and black lines indicate the reflection coefficient results of the ILMCA, DSCA, and w/o glass, respectively. This expressed bandwidth indicates that the total output power radiated from four patches is divided by the total input power entering four ports. As shown in Fig. 21(a), the bandwidth of the simulated DSCA and ILMCA antenna is 24–33 GHz. The bandwidth of the w/o glass is 26.3–28.9 GHz. Bandwidths of 26.5, 27, 27.5, and 28 GHz were selected as the representative values. Three types of array antenna's isolation characteristics are shown in Fig 21(a). In the graph, the solid line indicates ILMCA isolation, the dashed line indicates DSCA isolation and the dashed-dotted line represents the isolation of the w/o glass. As shown in the graph, the isolations of ILMCA, DSCA, and w/o glass in the 28-GHz band (24.5–29.5 GHz) have minimum values of −17, −14, and −15 dB, respectively.

The beam tilting performance of the three types of array antennas is shown in Fig. 21(b) and Table IX. Using four ways to assign phase differences, four beam tilting phenomena are observed in the figures. The three-color solid lines represent the simulation results when the phases of the ports are the same. The dashed lines represent the results when the phase difference of the four ports is 45°. Phases of 0°, 45°, 90°, and 135° are examples. The results when the phase difference of the four ports is 90° are denoted by a dashed-dotted line, and the result when the phase difference is 135° is shown

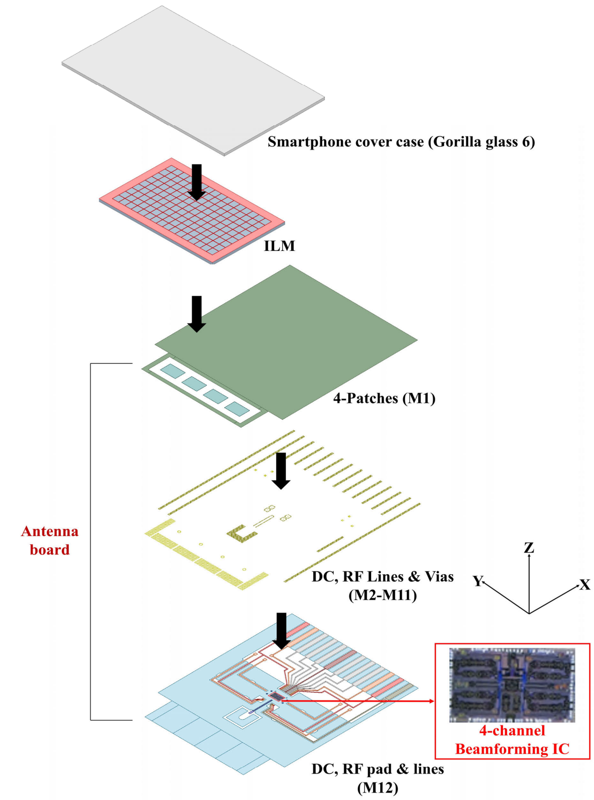

Fig. 22. Overall configuration diagram of the production version of the 1 × 4 ILMCAiP with a four-channel beamforming IC.

with dot lines. Comparing the results shown in Fig. 21(b) and Table IX, it is confirmed that the beam steering performance is improved owing to the metasurface insertion. When the beam is not tilted, the P.G of the ILMCA is 11.63 dBi and that of the DSCA is 10.94 dBi. Furthermore, the P.G of the ILMCA is 10.94 dBi and that of the DSCA is 7.29 dBi when the beam is tilted beyond 23°. These results imply that the ILM improves the beam coverage of array antennas.

V. Whole Configuration of AiP With 28-GHz Operating Four-Channel Beam Forming IC

Here, the beam steering performance of the AiP that combines a four-channel beamforming IC will be covered. In this study, AiP is significant in that it can realize an operating environment similar to an actual smartphone antenna because it combines a metasurface and a cover case, rather than simply combining an antenna and a beamforming IC. Therefore, if the metasurface improves the beam steering performance of the AiP; the beam coverage of the actual smartphone antenna may also be improved by the metasurface.

A. Design of AiP With Four-Channel Beamforming IC

Fig. 22 shows the production version of the 1 × 4 array ILMCAiP combined with four-channel beamforming IC. In this study, AiP consists of ILMCAiP and DSCAiP. As shown in Figs. 22 and 23, the AiP contains many elements (i.e., RF pads, dc pads, RF lines, dc lines, and vias). Multiple dc bias, phase control signal, and one-RF input signal should be assigned to beamforming IC for beam tilting operation.

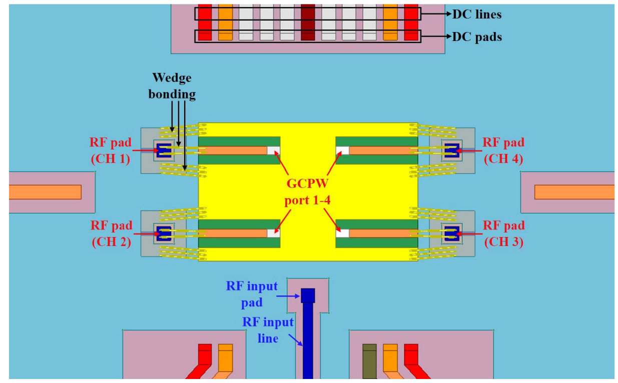

Fig. 23. Illustration of four GCPW ports of the 1 × 4 array-cased AiP for beam tilting performance in simulation.

TABLE XII
Summarized Beamforming IC Performances at 28 GHz

Frequency (GHz)	Input power (dBm)	Output power (dBm)	Gain (dB)
28	- 20	0.73	20.73
	- 10	10.02	20.02
	0	20.1	20.1
	1	20.49	19.49

In addition, four-RF output signals whose phases are revised by IC originate from four-output ports of beamforming IC. To put the four-RF output signals in four patches of the AiP board, output ports should be connected to the RF pads of the antenna. In this study, a four-channel beamforming IC is attached to the bottom layer [M12 in Fig. 20(d)]. Four-RF output ports and dc ports of the IC are connected to four RF pads and dc pads of the AiP board using wedge bonding. RF head for four patches of array antenna through wedge bonding, RF pad, lines, via, and indirect feeding lines. In addition, the phase controller and software program of the PC modulates the phase of four-RF signals inside the beamforming IC; therefore, four-RF output signals could come out with modulated phase. In the simulation, the roles of four-channel beamforming IC are substituted with four GCPW ports, as shown in Fig. 23. The GCPW ports are connected to each of the four RF pads by wedge bonding, and the performance is optimized. The phase of signals could be modulated using an EM simulation software (HFSS) so that the beam tilting phenomenon of AiP could be operated like in a real situation.

B. Simulation Result

The simulated beam tilting performances of the ILMCAiP and DSCAiP in the *YZ* plane are presented in Fig. 24 and Table X. It can be observed that the ILMCAiP performs better than the DSCAiP due to improved radiation performance by ILM. However, both types of array-cased AiP (ACAiP) with IC have lower P.G values than the cased antenna without IC due to bonding and line loss. In addition, the radiation pattern in the *YZ* plane is significantly reduced by the long ground with $+X$-direction.

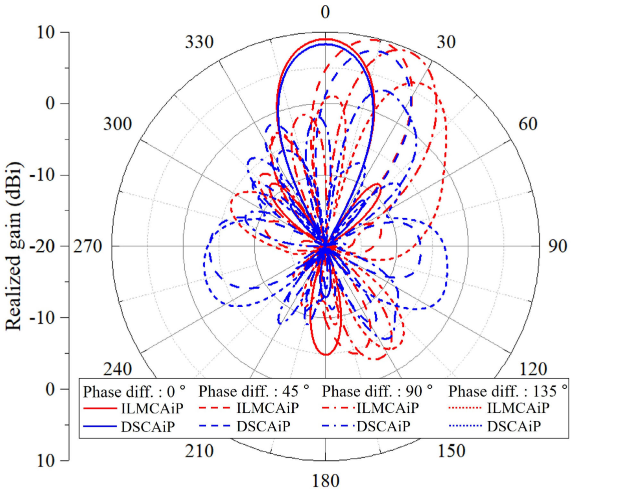

Fig. 24. Simulated beam tilting performances of the 1 × 4 array-cased AiP with four-channel beamforming IC in the *YZ* plane at 27 GHz.

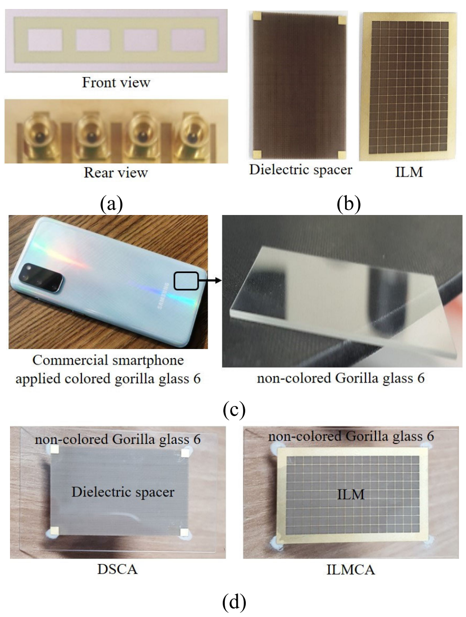

Fig. 25. Photographs of components of the 1 × 4 array-cased antennas. (a) 1 × 4 array antenna. (b) DS and ILM. (c) Smartphone cover case. (d) Front view of the DSCA and ILMCA.

Therefore, the P.G of the DSCAiP, which has a small gain toward the boresight, is further reduced when steering the beam.

VI. Fabrication and Measurement Results

Here, we verify the improvement of beam coverage performance by the metasurface through actual fabrication. Four modules are used: ILMCA, ILMCAiP, DSCA, and DSCAiP.

A. 1 × 4 Array-Cased Antenna

Fig. 25 shows the components of the two types of array-cased antennas. The 1 × 4 array antenna in Fig. 25(a) is fabricated from PCB stack-up technology and mini SMP connectors soldered to the rear side of the antenna are used as ports of the array antenna. DS and ILM are directly stacked

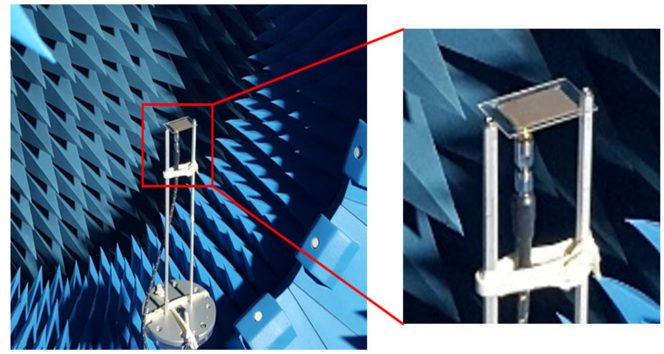

Fig. 26. Photograph of setup measuring radiation pattern performance of the 1 × 4 array-cased antenna.

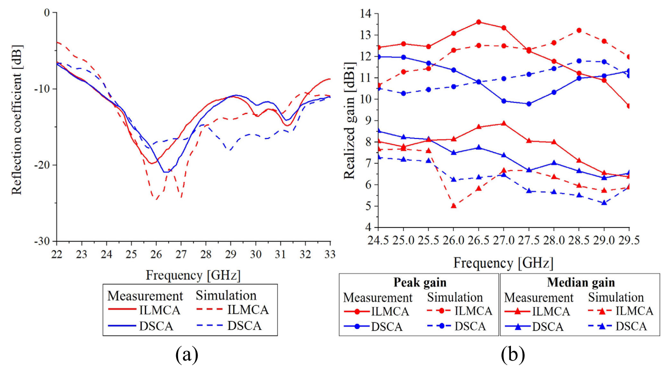

Fig. 27. Comparison of the 1 × 4 array-cased antenna simulation and measurement results. (a) Reflection coefficient and (b) gain.

and combined on the array antenna, respectively, and the cover case is placed on the modules to complete the cased antenna. Fig. 25(d) shows the products of the array DSCA and ILMCA produced using this process. Fig. 26 shows the setup measuring the radiation pattern of the array-cased antenna. The bandwidth of the radiation pattern measurable with this setup is 24.5–29.5 GHz, including some millimeter-wave (mm-wave) 5G band. The beam coverage of the array-cased antenna can be obtained by synthesizing the radiation patterns of each patch element [23], [24], [25], [26]. During this process, only one port of the patch to be measured is excited, and the ports of the other patches should be terminated with 50 Ω. The synthesized beam pattern calculated from this process represents the beam coverage of the array-cased antenna.

The measured bandwidth results of the array-cased antenna and the simulation results are presented in Fig. 27(a). The bandwidth of the DSCA is 23.5–33 GHz, while that of the ILMCA is 23.5–32.2 GHz, which includes n257 (26.5–29.5 GHz) and n258 (24.25–27.5 GHz) of FR2 bands. Based on these results, the fabricated array-cased antennas can be considered suitable for mm-wave 5G smartphone antennas. In addition, 26.5, 27, 27.5, and 28 GHz are selected as the representative frequencies. Fig. 27(b) shows the measured values of peak and M.Gs, which are the outcome of synthesizing the radiation pattern obtained from the setup presented in Fig. 26. The M.G is the gain in descending order based on the P.G in the hemisphere of the antenna radiating side. The Min. EIRP of the beam coverage can be obtained by adding the total input power to this value. The two largest measured P.Gs of the

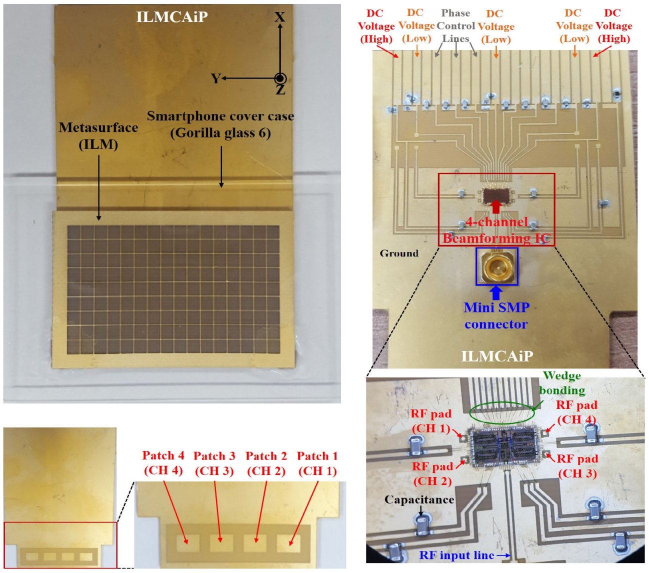

(a) (b)

Fig. 28. Photograph of the 1 × 4 array ILMCAiP with four-channel beamforming IC. (a) Front view. (b) Rear view.

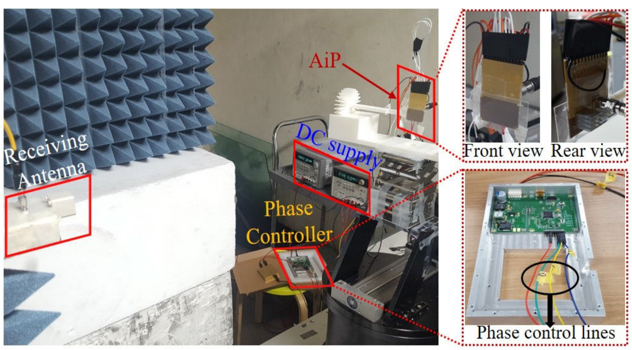

Fig. 29. Photograph of measurement setup on the beam tilting performance of the 1 × 4 ACAiP with four-channel beamforming IC.

ILMCA within the frequency bands are 13.62 dBi at 26.5 GHz and 13.35 dBi at 27 GHz. The P.Gs of the DSCA are 11.99 dBi at 24.5 GHz and 11.97 dBi at 25 GHz. Comparing the P.Gs of ILMCA and DSCA confirms that the ILM improves the maximum P.G. In addition, the M.G of the ILMCA is mostly higher than that of the DSCA or slightly lower than that of the DSCA in most bandwidths.

The comparison results indicate that the beam coverage of the ILMCA is better than that of DSCA. Although the frequency at which the maximum P.G of the simulated and fabricated antenna occurs was slightly shifted, in both cases, ILMCA had a larger gain than DSCA. This is due to the ILM's effect on increasing the P.G of the antenna by the ILM. Based on the comparison results, we conclude that the ILMCA's beam coverage performance is superior to that of the DSCA due to the contribution of ILM.

B. 1× 4 Array CAiP With Four-Channel Beamforming IC

Fig. 28 shows photographs of the fabricated 1 × 4 array ILMCAiP with 28-GHz operating four-channel beamforming IC [27]. The process of manufacturing is the same as that of the 1 × 4 array-cased antenna, except that the beamforming

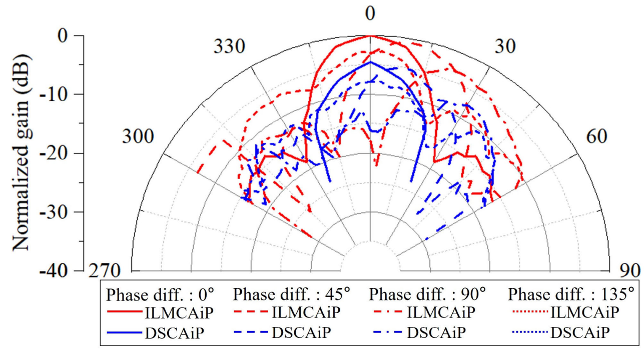

Fig. 30. Measured beam tilting performance of the 1 × 4 array CAiP with four-channel beamforming IC in the *YZ* plane at 28 GHz.

IC is attached below the AiP board and connecting signal lines with wedge bonding. Fig. 29 shows a photograph of the measurement setup for the beam tilting performance of the 1 × 4 array-cased AiP. As the devices to drive the IC are all contained in this measurement setup, it is more complicated compared with the setup of Fig. 26, which measures the radiation pattern of the array-cased antenna without IC. A signal generator introduces the intended signal to the AiP, and a spectrum analyzer measures receiving signal radiated from the AiP. Turning on the phase controller and providing dc bias to the AiP are the roles of dc supply in this setup. The phase controller and AiP are connected with phase control lines. Because AiP and IC are also connected with wedge bonding, the phase controller could manage the phase of the signal driving from IC to the four-patch of AiP. Using software installed on a PC, this study modulated the phase controller and obtained results of beam tilting performances.

The beam tilting performances of ACAiP in the *YZ* plane at 28 GHz are presented in Fig. 30 and Table XI in the form of a normalized gain. In the measurement, the input power entering the IC is −20 dBm, considering the breakdown of the IC. When an input power of −20 dBm is applied, the value of the output power from the IC is 0.73 dBm, and the gain of the chip is 20.73 dB, as summarized in Table XII. However, the values in Table XII are only the performances of the chip. If the chip is connected to the AiP board through wedge bonding, many obstacles downgrade the performance of the AiP. First, the loss of signals entering and exiting the chip occurs considerably owing to wedge bonding. Furthermore, a sensitive performance varies according to the shape of the bonding, and the difficulty of making the same shape of bonding as the simulation causes a disparity with the simulation results. Owing to these points, it is difficult to control the magnitude and phase difference of the signal entering each element patch of ACAiP. In addition, there is a phenomenon that the gain in the boresight direction of ACAiP is reduced by the long ground placed in the $+X$-direction in Fig. 28. In particular, DSCAiP does not have a metasurface that improves the gain in the boresight direction; therefore, it is significantly affected by asymmetric ground than ILMCAiP. Because of all the limitations, the beam tilting performance of the ILMCAiP and DSCAiP is not better than that of the ILMCA and DSCA, as shown in the comparison of Figs. 21 and 30. Therefore, the beam tilting phenomenon of the ILMCAiP and DSCAiP in the *YZ* plane is not observed when the phase difference between each element is the largest at 135°. Nevertheless, the beam coverage improvement effect by ILM can be sufficiently confirmed through a comparison of normalized gain. The boresight gain of the ILMCAiP with the largest P.G was set to 0 dB to normalize the P.G during beam steering. By comparing red lines with blue lines in Fig. 30 and analyzing the data in Table XI, it was established that the beam tilting performances of ILMCAiP surpass those of the DSCAiP. For example, when the beam is steered by 12°, the P.G of ILMCAiP is 4.27 dB higher than that of the DSCAiP. Comparing the measurement results, it can be observed that the ILM improves the beam tilting performance of the AiP.

VII. Conclusion

In this study, we propose innovative technologies to enhance the performance of 5G smartphone AiPs. By combining and optimizing the antenna, metasurface, and smartphone cover case simultaneously, we were able to minimize the negative effects of the cover case and obtain wide bandwidth and remarkable beam coverage. The operating circumstances of the developed AiP are similar to those of commercial smartphone antennas because the cover case is considered in the design step. In addition, the use of the metasurface significantly enhances the beam coverage. The developed antenna and metasurface are thin enough to be inserted into a smartphone and are directly connected without an air gap, making the proposed AiP practical for use in commercial smartphones. With these advantages, the method and technologies used to develop the proposed AiP could play a pioneering role in the research of 5G smartphone antennas.

Acknowledgment

The authors would like to thank Editage (www.editage.co.kr) for English language editing.

References

[1] R. Rodriguez-Cano, S. Zhang, K. Zhao, and G. F. Pedersen, "Mm-wave beam-steerable endfire array embedded in a slotted metal-frame LTE antenna," *IEEE Trans. Antennas Propag.*, vol. 68, no. 5, pp. 3685–3694, May 2020, doi: 10.1109/TAP.2020.2963915.

[2] J. Kurvinen et al., "Capacitively-loaded feed line to improve mm-wave and sub-6 GHz antenna co-existence," *IEEE Access*, vol. 8, pp. 139680–139690, 2020, doi: 10.1109/ACCESS.2020.3012773.

[3] R. Rodriguez-Cano, K. Zhao, S. Zhang, and G. F. Pedersen, "Handset frame blockage reduction of 5G mm-wave phased arrays using hard surface inspired structure," *IEEE Trans. Veh. Technol.*, vol. 69, no. 8, pp. 8132–8139, Aug. 2020, doi: 10.1109/TVT.2020.2996360.

[4] Y. Zhu, Z. Zhao, and C. Deng, "Millimeter-wave dual-polarized frame-integrated patch antenna array for 5G mobile handsets," in *Proc. IEEE 3rd Int. Conf. Electron. Inf. Commun. Technol. (ICEICT)*, Shenzhen, China, Nov. 2020, pp. 613–615, doi: 10.1109/ICEICT51264.2020.9334325.

[5] H. Kim and S. Nam, "Performance enhancement of 5G millimeter wave antenna module integrated tablet device," *IEEE Trans. Antennas Propag.*, vol. 69, no. 7, pp. 3800–3810, Jul. 2021, doi: 10.1109/TAP.2020.3044651.

[6] C. Di Paola, S. Zhang, K. Zhao, Z. Ying, T. Bolin, and G. F. Pedersen, "Wideband beam-switchable 28 GHz Quasi-Yagi array for mobile devices," *IEEE Trans. Antennas Propag.*, vol. 67, no. 11, pp. 6870–6882, Nov. 2019, doi: 10.1109/TAP.2019.2925189.

[7] K. K. So, B.-J. Chen, and C. H. Chan, "Microwave and millimeter-wave MIMO antenna using conductive ITO film," *IEEE Access*, vol. 8, pp. 207024–207033, 2020, doi: 10.1109/ACCESS.2020.3037900.

[8] B. Yu, K. Yang, C.-Y.-D. Sim, and G. Yang, "A novel 28 GHz beam steering array for 5G mobile device with metallic casing application," *IEEE Trans. Antennas Propag.*, vol. 66, no. 1, pp. 462–466, Jan. 2018, doi: 10.1109/TAP.2017.2772084.

[9] J. Seo et al., "Miniaturized dual-band broadside/endfire antenna-in-package for 5G smartphone," *IEEE Trans. Antennas Propag.*, vol. 69, no. 12, pp. 8100–8114, Dec. 2021, doi: 10.1109/TAP.2021.3088230.

[10] Y. Kim et al., "4 × 8 patch array-fed FR4-based transmit array antennas for affordable and reliable 5G beam steering," *IEEE Access*, vol. 7, pp. 88881–88893, 2019, doi: 10.1109/ACCESS.2019.2926379.

[11] I. Yoon and J. Oh, "Millimeter-wave thin lens using multi-patch incorporated unit cells for polarization-dependent beam shaping," *IEEE Access*, vol. 7, pp. 45504–45511, 2019, doi: 10.1109/ACCESS.2019.2909175.

[12] N. Hussain, M.-J. Jeong, A. Abbas, and N. Kim, "Metasurface-based single-layer wideband circularly polarized MIMO antenna for 5G millimeter-wave systems," *IEEE Access*, vol. 8, pp. 130293–130304, 2020, doi: 10.1109/ACCESS.2020.3009380.

[13] F. Costa, A. Monorchio, and G. Manara, "An overview of equivalent circuit modeling techniques of frequency selective surfaces and metasurfaces," *Appl. Comput. Electromagn. Soc. J.*, vol. 29, no. 12, pp. 960–976. Aug. 2014.

[14] D. Ferreira, R. F. S. Caldeirinha, I. Cuiñas, and T. R. Fernandes, "Square loop and slot frequency selective surfaces study for equivalent circuit model optimization," *IEEE Trans. Antennas Propag.*, vol. 63, no. 9, pp. 3947–3955, Sep. 2015, doi: 10.1109/TAP.2015.2444420.

[15] W. Yang, S. Chen, Q. Xue, W. Che, G. Shen, and W. Feng, "Novel filtering method based on metasurface antenna and its application for wideband high-gain filtering antenna with low profile," *IEEE Trans. Antennas Propag.*, vol. 67, no. 3, pp. 1535–1544, Mar. 2019, doi: 10.1109/TAP.2018.2889028.

[16] Y. M. Pan, P. F. Hu, X. Y. Zhang, and S. Y. Zheng, "A low-profile high-gain and wideband filtering antenna with metasurface," *IEEE Trans. Antennas Propag.*, vol. 64, no. 5, pp. 2010–2016, May 2016, doi: 10.1109/TAP.2016.2535498.

[17] W. Liu, Z. N. Chen, and X. Qing, "Metamaterial-based low-profile broadband aperture-coupled grid-slotted patch antenna," *IEEE Trans. Antennas Propag.*, vol. 63, no. 7, pp. 3325–3329, Jul. 2015, doi: 10.1109/TAP.2015.2429741.

[18] M. A. Meriche, A. Messai, H. Attia, B. Hammache, and T. A. Denidni, "High-gain wideband Fabry-Pérot slot antenna with partially reflective surface," in *Proc. 16th Medit. Microw. Symp. (MMS)*, Nov. 2016, pp. 1–4, doi: 10.1109/MMS.2016.7803833.

[19] A. R. Vaidya, R. K. Gupta, S. K. Mishra, and J. Mukherjee, "Effect of superstrate height on gain of MSA fed Fabry Pérot cavity antenna," in *Proc. Loughborough Antennas Propag. Conf.*, 2011, pp. 1–4, doi: 10.1109/LAPC.2011.6114018.

[20] J. Oh, "Millimeter-wave short-focus thin lens employing disparate filter arrays," *IEEE Antennas Wireless Propag. Lett.*, vol. 15, pp. 1446–1449, 2016, doi: 10.1109/LAWP.2015.2512853.

[21] J. Lee, "Compact and robust Fabry–Pérot cavity antenna with PEC wall," *J. Electromagn. Eng. Sci.*, vol. 21, no. 3, pp. 184–188, Jan. 2021, doi: 10.26866/jees.2021.3.r.25.

[22] C. H. S. Nkimbeng, H. Wang, and I. Park, "Coplanar waveguide-fed bidirectional same-sense circularly polarized metasurface-based antenna," *J. Electromagn. Eng. Sci.*, vol. 21, no. 3, pp. 210–217, Jul. 2021, doi: 10.26866/jees.2021.3.r.28.

[23] A. K. Bhattacharyya, *Phased Array Antennas: Floquet Analysis, Synthesis, BFNs and Active Array Systems*, vol. 179. Hoboken, NJ, USA: Wiley, 2006.

[24] D. F. Kelley and W. L. Stutzman, "Array antenna pattern modeling methods that include mutual coupling effects," *IEEE Trans. Antennas Propag.*, vol. 41, no. 12, pp. 1625–1632, Dec. 1993, doi: 10.1109/8.273305.

[25] D. M. Pozar, "The active element pattern," *IEEE Trans. Antennas Propag.*, vol. 42, no. 8, pp. 1176–1178, Aug. 1994, doi: 10.1109/8.310010.

[26] M. H. Novak, F. A. Miranda, and J. L. Volakis, "Ultra-wideband phased array for millimeter-wave ISM and 5G bands, realized in PCB," *IEEE Trans. Antennas Propag.*, vol. 66, no. 12, pp. 6930–6938, Dec. 2018, doi: 10.1109/TAP.2018.2872177.

[27] J. Park, S. Lee, D. Lee, and S. Hong, "9.8 A 28 GHz 20.3%-transmitter-efficiency 1.5°-phase-error beamforming front-end IC with embedded switches and dual-vector variable-gain phase shifters," in *IEEE Int. Solid-State Circuits Conf. (ISSCC) Dig. Tech. Papers*, Feb. 2019, pp. 176–178, doi: 10.1109/ISSCC.2019.8662512.

Jaebaek Jung (Student Member, IEEE) received the B.S. degree in electronic and electrical engineering from POSTECH, Pohang, South Korea, in 2012. He is currently pursuing the integrated master's and Ph.D. degrees with the Department of Electrical Engineering and Computer Science, Seoul National University, Seoul, South Korea.

His current research interests include metasurface, 5G, 6G, and antenna-in-package (AiP).

Woojun Lee (Student Member, IEEE) received the B.S. degree in electrical and computer engineering from Seoul National University, Seoul, South Korea, in 2021, where he is currently pursuing the M.S. degree in electrical and computer engineering.

His current research interests include wideband antenna, 5G, 6G, and antenna-in-package (AiP).

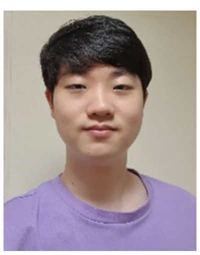

Gyuha Lee (Graduate Student Member, IEEE) received the B.S. degree in electrical engineering from Hanyang University, Seoul, South Korea, in 2020, and the M.S. degree in electrical engineering from the Korea Advanced Institute of Science and Technology, Daejeon, South Korea, in 2022, where he is currently pursuing the Ph.D. degree in electrical engineering.

His current research interests include millimeter wave (mm-wave)-integrated circuits and phased-array systems for wireless communications.

Songcheol Hong (Member, IEEE) received the B.S. and M.S. degrees in electronics engineering from Seoul National University, Seoul, South Korea, in 1982 and 1984, respectively, and the Ph.D. degree in electrical engineering and computer science from the University of Michigan, Arbor, MI, USA, in 1989.

He visited the EECS Department, Stanford University, Stanford, CA, USA, as a Visiting Professor, in 1997. He was with Samsung Microwave Semiconductor, Milpitas, CA, USA. He served as a Dean for research affairs and the Director for KI-IT Convergence at the Korea Advanced Institute of Science and Technology (KAIST), Daejeon, South Korea. He is currently the Director of the Millimeter Wave Radar-Communication Research Center (MiraCom-RC) supported by the Korean Government. He is currently a Professor with the School of Electrical Engineering, KAIST, where he is also a KT-Chaired Professor. He authored or coauthored more than 300 technical articles and 150 patents. His research interests include RFICs and especially in millimeter-wave (mm-wave) front-end ICs for 5G communications and intelligent high-resolution radars.

Dr. Hong received the Qualcomm Faculty Award in 2019. He is currently a member of National Academy of Engineering of Korea (NAEK), Korean Institute of Electromagnetic Engineering and Science (KIEES), and Korea Institute of Telematics and Electronics (KITE). He has served as a Board Member for Techno-Park of Daejeon Metropolitan city for 15 years. He served as the General Chair for Radio-Frequency Integration Technology (RFIT) 2017 supported by IEEE and TPC chairs of Asia-Pacific Microwave Conference (APMC) 2013 and Global Symposium on Millimeter-Waves and Terahertz (GSMM) 2014.

Jungsuek Oh (Senior Member, IEEE) received the B.S. and M.S. degrees from Seoul National University, Seoul, South Korea, in 2002 and 2007, respectively, and the Ph.D. degree from the University of Michigan at Ann Arbor, Ann Arbor, MI, USA, in 2012.

From 2007 to 2008, he was a Hardware Research Engineer with Korea Telecom, Seoul, working on the development of flexible RF devices. From 2013 to 2014, he was a Staff RF Engineer with Samsung Research America, Dallas, TX, USA, working as a Project Leader for the 5G/millimeter-wave (mm-wave) antenna system. He is currently an Associate Professor with the School of Electrical and Computer Engineering, Seoul National University. He has authored or coauthored more than 60 technical journals and conference papers. His current research interests include mm-wave beam focusing/shaping techniques, antenna miniaturization for integrated systems, and radio propagation modeling for indoor scenarios.

Dr. Oh was a recipient of the 2011–2012 Rackham Predoctoral Fellowship Award, the 2014 Samsung DMC Research and Development Innovation Award, the 2018 SNU Creative Researcher Award, the 2019 Samsung Electro-Mechanics Silver Prize, and the best paper awards from several conferences. He has served as a TPC member and as a Session Chair for the IEEE AP-S/USNC-URSI and ISAP.